EFFECTS OF HYPER HEMISPHERICAL FIELD IN BUNDLE ADJUSTMENT WITH FISHEYE IMAGES

A. M. G. Tommaselli [1] *, T. A. C. Garcia [1], L. F. Castanheiro[1], M. B. Campos[2], G. H. dos Santos[1]

[1] Department of Cartography, Faculty of Sciences and Technology, São Paulo State University (UNESP), São Paulo 19060-900, Brazil {a.tommaselli, thaisa.correia, leticia.ferrari, guilherme.h.santos}@unesp.br

[2] Department of Remote Sensing and Photogrammetry, Finnish Geospatial Research Institute (FGI), National Land Survey of Finland, Espoo, mariana.campos@maanmittauslaitos.fi

KEY WORDS: Fisheye camera, Hyper Hemispherical lenses, bundle adjustment, Mobile Mapping, Backpack platform.

ABSTRACT:

The large field of view and compact structure make fisheye lens cameras an attractive technology for mobile mapping systems and visual navigation. Fisheye cameras usually have a field of view equal to or higher than 180º. Lenses that can capture light rays coming from angles larger than 180º are known as hyper hemispherical lenses. Some of the existing mathematical models can be unsuitable for those points beyond the 180º field of view when performing photogrammetric processes based on these equations, underexploring the full potential of fisheye lens cameras. In this case, depending on the selected projection model, points appearing in the hyper hemispherical (HH) field can produce blunders in the bundle adjustment. Nevertheless, most of the available solutions for camera calibration and bundle adjustment were implemented using the equidistant model. Therefore, the points located in the hyper hemispherical field are often removed from the bundle adjustment either during keypoint detection or by applying a mask to remove the entire HH field from the images. In this paper, we assessed experimentally the hypothesis that using the original HH full-field image introduces blunders, deteriorating the bundle adjustment. The experiments were performed with a Ricoh Theta S 360º camera which was mounted on a backpack platform. The camera was set in video mode, and frames were captured at a rate of 1 fps, while traversing an urban street, generating 307 frames. Experiments were performed, including or removing HH points in the bundle adjustment. The results show that the errors in the dataset with the hyper hemispherical field were larger than the ones using cropped images.

1. INTRODUCTION

Omnidirectional systems have become more reliable and efficient, being used in many applications, including those requiring high geometric accuracy. Some applications focus only on visual quality with fewer requirements for high accuracy, such as visualisation of landscapes and indoor buildings, surveillance, action scenes, recording of forest stand hemispheres (Schwalbe, 2005), and many others. However, being able to produce an accurate geometric 3D reconstruction of the environment is a key feature for a mobile mapping system.

Omnidirectional systems provide a wide field of view (usually 360º), and several different types of optical components are used to produce such systems. Catadioptric system combines projective cameras with mirrors, while fisheye cameras rely on refractive elements. Omnidirectional images can also be generated by rotating cameras and mosaicking images acquired by multiple synchronised cameras. Fisheye and catadioptric systems can capture a full hemisphere in a single image shot, which solves the problem of synchronisation and avoid mosaicking multiple images.

Due to the large field of view, compact structure and reduced operational and computational costs for navigation, fisheye lens cameras have been frequently used in positioning and navigation, sometimes combined with other sensors, such as LiDAR, Global Navigation Satellite Systems (GNSS) receivers and inertial measurement units (IMU). This sensor's integration can overcome challenges such as occlusion, dynamic object detection, and GNSS-denied locations (Alatise and Hancke, 2020).

Visual-inertial navigation, especially using fisheye cameras plays a key role in multi-sensors mobile systems, improving navigation performance in different environmental conditions. For instance, in the last years, many portable platforms, such as robots (Flögel et al., 2022), UAVs (Lin et al., 2018; Gao et al., 2020), autonomous cars (Heng et al., 2019, Eising et al., 2022) or backpacked systems (Campos et al., 2018b) have benefited from fisheye cameras.

Fisheye cameras usually have a field of view of 180º, but there are lenses that can capture light rays coming from larger angles. Pernechele (2016) coined the term hyper hemispherical lenses (HH lenses) to describe a lens system which looks 360º around the azimuthal axis and tens of degrees above the horizon. This development has opened new possibilities, such as using two cameras to cover the whole viewing sphere. However, modelling hyper hemispherical lenses (HH lenses) is still a concern continuously discussed (Campos et al., 2018b; Martins et al., 2020; Castanheiro et al., 2021; Lichti et al., 2021).

The knowledge of the internal camera geometry allows a suitable photogrammetric treatment of the images, and highly accurate results can be achieved, provided that rigorous calibration with a suitable model is used. Therefore, points in the hyper

* Corresponding author

hemispherical field have to be correctly modelled, making it possible to take advantage of the full potential of fisheye lens. For instance, assembling two fisheye cameras in a back-to-back mount provides full 360º coverage, which has been explored by recent commercial omnidirectional camera systems. Several manufacturers of action camera are releasing such a solution (Ricoh, 2023; GoPro, 2023; Insta360, 2023). However, in these dual-fisheye mounts, the lenses and their entrance pupils have to be physically displaced and, as a consequence, some occluded areas are likely to occur if hemispherical fisheye lenses are used. To avoid this problem, when using dual-fisheye cameras, each fisheye lens has to cover more than 180º, which requires HH lenses (Pernechele, 2016).

Nevertheless, most of the available solutions for camera calibration and bundle adjustment were only implemented using the equidistant model, which cannot handle the hyper hemispherical field. Then, the points located in the HH field end up to be removed from the bundle adjustment (Perfetti e al., 2018, Campos et al., 2018a). Especially for professional use, there are photogrammetric software that have already implemented fisheye projection models. A well-known is Agisotf Metashape (Agisoft, 2023a) which implements a complete photogrammetric pipeline from the initial relative orientation, in-situ camera calibration, generation of dense surface models and ortho-mosaics, using the equidistant projection model.

This paper aims to experimentally study the loss of accuracy when using the original hyper hemispherical images in the bundle adjustment with the equidistant model and the strategies to overcome this problem.

2. BACKGROUND

2.1 Mathematical model for fisheye cameras

The geometric treatment of fisheye images can be done either by rigorous and physical-based mathematical models (Abraham and Förstner, 2005; Schneider et al., 2009; Hughes et al., 2010; Campos et al., 2018b; Lichti et al., 2021) or by generalised models (Courbon et al., 2007; Geyer and Daniilidis, 2000; Kedzierski et al., 2006; Khomutenko et al., 2016; Usenko et al., 2018).

The more common projection models are perspective, equidistant (Equation 1), equisolid-angle (Equation 2), stereographic (Equation 3), and orthogonal (Equation 4). The perspective projection considers that an incident light ray reaching the lens will emerge with the same angle. Considering r_p as the radial distance, f as the camera focal length, and α as the incident ray angle, the perspective model is given as $r_p = f.\ tan\ (\alpha)$. This model is unsuitable for fisheye lenses since r_p will approach to the infinite as α approaches 90º . Equations (1) to (4) present projection models for fisheye lenses.

Equidistant:	$r_p = f.\ \alpha$	(1)
Equisolid-angle:	$r_p = 2.f.\ sin\ (\alpha/2)$	(2)
Stereographic	$r_p = 2.f.\ tan\ (\alpha/2)$	(3)
Orthogonal	$r_p = f.\ sin\ (\alpha)$	(4)

These projection models presented in Equations (1) to (4) can be expanded as observation equations and distortion models (Abraham and Förstner, 2005; Schneider et al., 2009; Campos et al., 2018b). The observation equations for the equidistant model (Schneider et al., 2009) are shown in Equation (5):

$$x = f.\frac{X_c}{\sqrt{{X_c}^2+{Y_c}^2}}.tan^{-1}\frac{\sqrt{{X_c}^2+{Y_c}^2}}{Z_c}$$
$$y = f.\frac{Y_c}{\sqrt{{X_c}^2+{Y_c}^2}}.tan^{-1}\frac{\sqrt{{X_c}^2+{Y_c}^2}}{Z_c} \quad (5)$$

In which:
X_c, Y_c, Z_c are 3D coordinates of a point in the camera reference system;
f is the camera focal length;
x, y are the coordinates projected to the image plane and correspond to the observed values, already reduced to the principal point and corrected for the lens distortion effects with the well-known Conrady-Brown model.

The transformation of X_c, Y_c, Z_c to ground coordinates (X, Y, Z) requires a rigid body geometric transformation as a function of the camera position and attitude (Exterior orientation).

As previously mentioned, some of the existing mathematical models can be unsuitable for those points beyond the 180º field of view when performing photogrammetric processes based on these equations. Using points appearing in the hyper hemispherical (HH) field can produce blunders in the bundle adjustment, depending on the selected projection model, as shown by Castanheiro et al. (2021) for a calibration problem. The authors compared experimentally the more common projection models (equidistant, equisolid-angle, stereographic, and orthogonal) for hyper hemispherical images acquired with a Ricoh Theta dual-fisheye camera, concluding that the equisolid-angle model presented the best results in the simultaneous calibration experiments. They also concluded that the use of equidistant projection model can cause an incorrect mapping of the hyper hemispherical points in the image plane due to the *atan* function in the observation equations (Castanheiro et al., 2021).

Nevertheless, Agisotf Metashape (Agisoft, 2023a) software uses the equidistant projection model (Agisoft, 2023, pg. 138) for camera calibration and bundle adjustment with fisheye images. Equations (8) are the projection models implemented in Agisoft Metashape Pro (Agisoft, 2023, pg. 138), with some minor modifications in the notation.

$$x_p = \frac{X_c}{Z_c}$$
$$y_p = \frac{Y_c}{Z_c} \quad (6)$$

$$r_p = \sqrt{x_p^2 + y_p^2} \quad (7)$$

$$x = f.x_p.\frac{tan^{-1}(r_p)}{r_p}$$
$$y = f.y_p.\frac{tan^{-1}(r_p)}{r_p} \quad (8)$$

In which; x_p, y_p are intermediate projected coordinates (*tan* function of the viewing angles, or coordinates considering a unit focal length);
r_p is the radial distance;
x, y are the coordinates projected to the image plane, with the equidistant condition, and;
f is the camera focal length.

Equations (9) describe the radial symmetric and decentering distortion corrections, in which the higher order terms (P_3 and P_4) were neglected.

$$x' = x(1 + K_1r^2 + K_2r^4 + K_3r^6 + K_4r^8) + (P_1(r^2 + 2x^2) + 2P_2xy)$$
$$y' = y(1 + K_1r^2 + K_2r^4 + K_3r^6 + K_4r^8) + (P_2(r^2 + 2y^2) + 2P_1xy) \quad (9)$$

$$r = \sqrt{x^2 + y^2} \quad (10)$$

In which, K_1, K_2, K_3, K_4 are the radial symmetric distortion coefficients, P_1, P_2 are the coefficients for decentering distortion.

Equations (11) relates the coordinates projected to the image space with the image coordinated (u and v) and can be used as observation equations.

$$u = \frac{w}{2} + c_x + x'.f + x'B_1 + y'B_2$$
$$v = \frac{h}{2} + c_y + y'.f \quad (11)$$

In which: u and v are the point coordinates in the image coordinate system (in pixels); w, h are the image width and height in pixels; B_1 and B_2 are the affinity and skew coefficients; c_x and c_y are the coordinates of the principal point.

After some manipulations, Equation (5) (Schneider et al., 2009) can be obtained from equations (6), (7) and (8). As previously mentioned, points in the hyper hemispherical field do not fit equations (8) and, thus, can generate a blunder. In this specific case, to mitigate this problem, the points located in the hyper hemispherical field have to be removed from the bundle adjustment. Another option is to apply a mask to remove the entire HH field from the images.

2.2 Fisheye cameras and backpacked systems

Fisheye and panoramic cameras are affordable alternatives for compact and lightweight mobile mapping systems, such as backpacks and handheld mobile mapping platforms. Those systems have been extensively used for mobile mapping in difficult access environments, such as forests (Campos et al., 2018a), urban canyons (Eising et al., 2022), indoor navigation (Kim et al., 2021), cultural heritage documentation (Barazzetti et al., 2017) (Perfetti et al., 2018), tunnels and caves inspection (Alessandri et al., 2019; Meyer et al., 2020).

Panoramic spherical cameras, such as Ladybug 5, have been explored in backpacked mobile mapping systems (Rau et al., 2016; Blaser et al., 2018; Blaser et al., 2021) and camera rigs (Ji et al., 2020). More recently, Perfetti and Fassi (2022) developed a handheld multi-camera system containing five industrial-grade cameras (Flir BFS 50S5) and a small backpack for power supply and computer. The system was used to map narrow spaces at Milan's Cathedral (e.g. spiral staircase). However, the use of many cameras increases the complexity of camera synchronisation and poses further problems with the generation of a single panoramic image from multiple viewpoints.

An alternative is the use of fisheye lens cameras, in which fewer cameras are needed to produce a wider panorama. Campos et al. (2018b) developed a backpack system composed of a dual-fisheye camera (Ricoh Theta S) and a low-cost navigation system for forest mapping and stem detection. Other commercial dual-fisheye cameras, such as Samsung Gear 360, and XiaoMi Mi Sphere have also been explored at handheld mobile setups for cultural heritage and tunnel structural monitoring (Koehl et al., 2016; Barazzetti et al., 2017; Sun and Zhang, 2019).'

Fisheye cameras are often combined in backpack mobile mapping systems with other optical remote sensors, such as laser scanners, as presented by Corso and Zakhor (2013), Kim (2013) and Liang et al. (2013).

3. METHODOLOGY

The study area is a street inside the campus surrounded by buildings and vegetation with a path 140 m long. The experiments were performed with a Ricoh Theta S 360º camera (Fig.1.a) (Ricoh, 2023), which was mounted on a backpack platform (Fig 1.b). The camera was assembled in a handheld gimbal for stabilisation. A navigation GNSS receiver and an IMU (UBLOX NEO6M) were attached to provide an initial trajectory. Technical specifications of the Ricoh Theta S camera are presented in Table 1.

Figure 1. (a) The backpack mount, (b) Ricoh Theta S dual-fisheye camera, (c) MPU IMU, and; (d) UBLOX GNSS receiver.

Camera	Ricoh Theta S
Sensor size	Two 1/2·3" CMOS Sensors (14 Mpx)
Still Image	2688 x 2688 pixels in each sensor
Dual fisheye Image	960 x 1080 pixels in each sensor
Fisheye field of view	190° each
Nominal focal length	1.31 mm
Pixel size	5 µm

Table 1: Technical specifications of the Ricoh Theta S digital camera.

The calibration of the Ricoh Theta S camera was previously performed by Campos et al. (2018b) using the equidistant model and relative orientation stability constraints. The estimated interior orientation parameters of sensor 2, used in this experiment, are presented in Table 2.

Parameter	Estimated value	Estimated standard deviation
f (mm)	1.4295	0.0012
x_0 (mm)	0.0042	0.0008
y_0 (mm)	0.2934	0.0010
k_1 (mm^{-2})	-16.0 E-3	1.2 E-3
k_2 (mm^{-4})	6.26 E-3	5.0 E-4
k_3 (mm^{-6})	-1.19 E-3	6.63 E-5
P_1 (mm^{-1})	-7.13 E-4	6.12 E-5
P_2 (mm^{-1})	-1.29 E-4	7.32 E-5

Table 2: Interior orientation parameters (IOP) of the Ricoh Theta S digital camera obtained with the equidistant model Campos et al. (2018b).

Two image datasets were generated for the experiments aiming to investigate the effects of hyper hemispherical points in the bundle adjustment with the equidistant model. The first uses the original hyper hemispherical images (Fig.2.a), while the second dataset uses cropped images, in which the hyper hemispherical fields were removed (Fig. 2.b). The camera captures dual fisheye images with 29 fps (frames per second). From the dual-fisheye frames captured, only fisheye images from one sensor were selected with 1 fps rate to be used in this study. Both datasets have 307 frames and the same data acquisition setup.

Natural and signalised control points were surveyed with GNSS-RTK for comparative analysis. Fig. 3 depicts the position of the Ground Control Points (GCPs) and the camera locations. These two image datasets were processed with Agisoft Metashape Pro, using simultaneous bundle adjustment with the fisheye camera model. The surveyed ground points were used in two combinations of the GCPs and Check Points (ChP): 26 GCPs and 4 ChP; and 20 GCPs and 10 ChP.

Experiments with different sets of Interior Orientation Parameters (IOPs) were also conducted. The bundle adjustment was calculated with previously estimated IOPs which were considered fixed in the bundle adjustment (Table 2), and with in-situ calibration, which was performed with Metashape tool. The values presented in Table 2 were imported using the Australis format and converted internally to the Agisoft model (Equations 9 and 11).

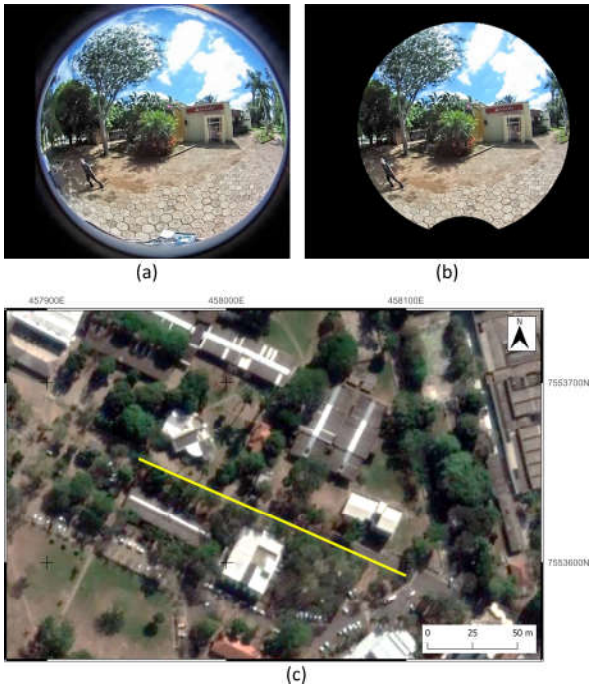

Figure 2. Fisheye images used in the experiments: (a) original frame with the hyper hemispherical field and; (b) with 180º field; (c) trajectory followed by the backpacked platform.

4. RESULTS AND DISCUSSION

The results of the experiments are summarised in Tables 3, 4, 5 and 6, with the Root Mean Square Error (RMSE) of GCPs and ChP. In these tables, the first group of results show the RMSE when using the original images, including the HH field, and the second group uses the cropped images.

Tables 3 and 4 summarise the results with previous IOPs with two combinations of GCPs and ChP and images with and without the HH field.

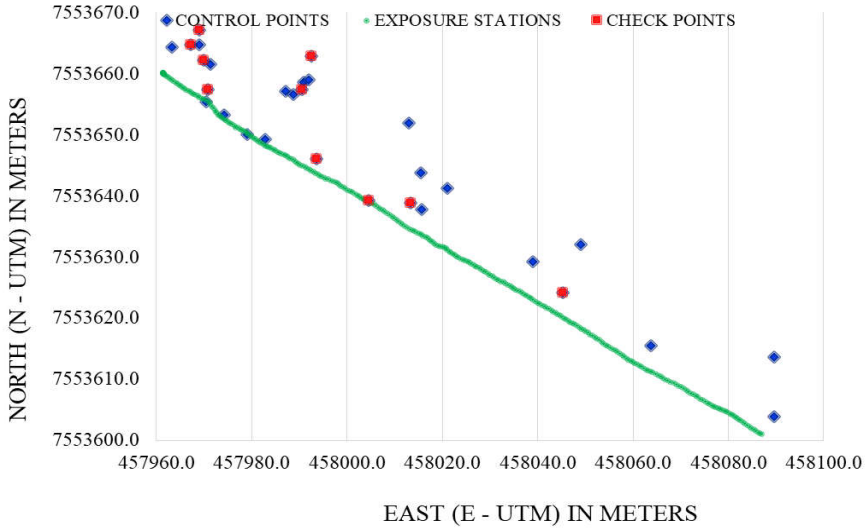

Figure 3. Configuration of exposure stations, control and check points.

Data set 1: Original hyper hemispherical images				
	Number of points	RMSE_X (cm)	RMSE_Y (cm)	RMSE_Z (cm)
GCP	26	14.8	11.7	6.6
Check points	4	19.8	27.6	6.9
Data set 2: Cropped images, without the HH field				
GCP	26	1.9	1.8	2.1
Check points	4	17.6	11.4	7.7

Table 3: RMSE in 26 GCPs and 4 ChP after the bundle adjustment with fixed IOPs.

Data set 1: Original hyper hemispherical images				
	Number of points	RMSE_X (cm)	RMSE_Y (cm)	RMSE_Z (cm)
GCP	20	14.8	15.0	7.4
Check points	10	17.6	13.2	6.1
Data set 2: Cropped images without the HH field				
GCP	20	1.6	1.5	1.8
Check points	10	6.2	6.6	5.8

Table 4: RMSE in 20 GCPs and 10 ChP after the bundle adjustment with fixed IOPs.

Data set 1: Original hyper hemispherical images				
	Number of points	RMSE_X (cm)	RMSE_Y (cm)	RMSE_Z (cm)
GCP	26	7.7	12.2	3.9
Check points	4	7.9	6.3	4.5
Data set 2: Cropped images without the HH field				
GCP	26	3.9	5.9	2.3
Check points	4	5.9	3.1	1.8

Table 5: RMSE in 26 GCPs and 4 ChP after the bundle adjustment with **in-situ calibration**.

Data set 1: Original hyper hemispherical images				
	Number of points	RMSE_X (cm)	RMSE_Y (cm)	RMSE_Z (cm)
GCP	20	5.9	5.1	3.5
Check points	10	9.0	7.2	5.1
Data set 2: Cropped images without the HH field				
GCP	20	2.0	1.6	2.0
Check points	10	2.8	5.9	2.4

Table 6: RMSE in 20 GCPs and 10 ChP after the bundle adjustment with **in-situ calibration**.

The results show that the errors in the bundle adjustment using the dataset with the hyper hemispherical field were larger than the ones using cropped images in all configurations of GCPs and ChP, and IOPs sets. This happens because the points in the hyper hemispherical field do not fit the equidistant model used in Metashape. In Table 3, the magnitude of the RMSEs in ChPs are still large for the dataset without the HH field due to large error in one single check point. Thus, the results show that cropping the hyper hemispherical field solves the problem at the cost of reducing the covered field.

Figure 4 depicts the trajectory (in blue) with the exposure stations, the position of the 10 ChPs (in red), and the magnitude and direction of the planimetric discrepancies (E, N), based on the experiment using fixed IOPs without the HH field. The ChPs showed similar discrepancies, as can be observed in Figure 4. However, in the first third part of the trajectory (highlighted with a yellow circle, in Fig. 4), the check points exhibited slightly larger discrepancies, possibly due to the geometry of these points, which are very close to the exposure station, which unfavourably affects the intersection geometry of the points in object space.

An important remark refers to the IOPs used in the bundle adjustment. Existing parameters from a previous calibration were considered fixed in the bundle adjustment resulting in discrepancies in the check points (Tables 3 and 4) slightly larger than those achieved with in-situ calibration (Tables 5 and 6). In this case, a large number of GCPs were available, thus favouring the use of in-situ calibration, but in practical applications, it is not common to have a dense network of GCPs.

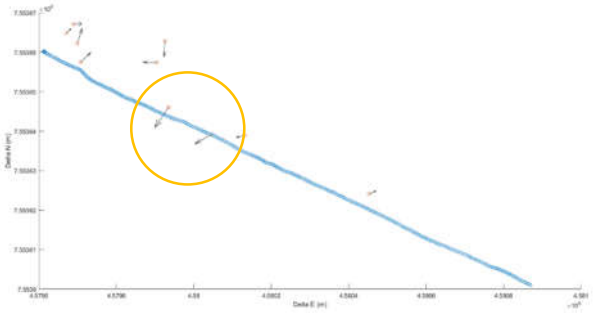

Figure 4. Exposure stations and error vectors of the check points.

5. CONCLUSIONS

In this paper, we have experimentally assessed the loss of accuracy when using the original hyper hemispherical images in the bundle adjustment with the equidistant in the Agisoft Metashape. It was shown that cropping the HH field solves this problem.

The main alternative to solve this issue, as presented by Castanheiro et al. (2021) is to use the equisolid model in the bundle adjustment with the Conrady-Brown distortion parameters. Another option is to use the equirectangular images produced by Ricoh Theta, but these images are already corrected for the tilt, and this would affect the image geometry. This hypothesis was not tested and is being left as a suggestion for future work. Another suggestion is to study the use of accurate coordinates of the exposure stations supplied by an onboard GNSS receiver.

ACKNOWLEDGEMENTS

This study was funded by the Coordenação de Aperfeiçoamento de Pessoal de Nível Superior - Brasil (CAPES) (Finance Code 88887.310313/2018-00 and 88881.310314/2018-01), the National Council for Scientific and Technological Development – CNPq (grant n. 303670/2018-5) and the São Paulo Research Foundation – FAPESP (grant n. 2021/06029-7).

REFERENCES

Abraham, S., Förstner, W., 2005. Fish-eye-stereo calibration and epipolar rectification. *ISPRS Journal of Photogrammetry and Remote Sensing* 59, 278–288. http://dx.doi.org/10.1016/j.isprsjprs.2005.03.001

Agisoft, 2023a. MetaShape. URL https://www.metashape-la.com/en/home/ (accessed 2.11.23).

Agisoft, 2023b. Agisoft Metashape User Manual - Professional Edition, Version 1.5.

Alatise, M.B., Hancke, G.P., 2020. A Review on Challenges of Autonomous Mobile Robot and Sensor Fusion Methods. *IEEE Access* 8, 39830–39846. https://doi.org/10.1109/ACCESS.2020.2975643

Alessandri, L., Baiocchi, V., Del Pizzo, S., Rolfo, M.F., Troisi, S., 2019. Photogrammetric survey with fisheye lens for the characterisation of the la Sassa Cave. *Int. Arch. Photogramm. Remote Sens. Spatial Inf. Sci.* XLII-2/W9, 25–32. https://doi.org/10.5194/isprs-archives-XLII-2-W9-25-2019

Barazzetti, L., Previtali, M., Roncoroni, F., 2017. 3D MOdelling with the SAMSUNG GEAR 360. *Int. Arch. Photogramm. Remote Sens. Spatial Inf. Sci*. XLII-2/W3, 85–90. https://doi.org/10.5194/isprs-archives-XLII-2-W3-85-2017

Blaser, S., Cavegn, S., Nebiker, S., 2018. Development of a portable high performance mobile mapping system using the robot operating system. *ISPRS Ann. Photogramm. Remote Sens. Spatial Inf. Sci.* IV–1, 13–20. https://doi.org/10.5194/isprs-annals-IV-1-13-2018

Blaser, S., Meyer, J., Nebiker, S., 2021. Open urban and forest datasets from a high-performance mobile mapping backpack – a contribution for advancing the creation of digital city twins. I*nt. Arch. Photogramm. Remote Sens. Spatial Inf. Sci*. XLIII-B1-2021, 125–131. https://doi.org/10.5194/isprs-archives-XLIII-B1-2021-125-2021

Campos, M.B., Tommaselli, A.M.G., Honkavaara, E., Prol, F. dos S., Kaartinen, H., El Issaoui, A., Hakala, T., 2018a. A Backpack-Mounted Omnidirectional Camera with Off-the-Shelf Navigation Sensors for Mobile Terrestrial Mapping: Development and Forest Application. *Sensors* 18. https://doi.org/10.3390/s18030827

Campos, M.B., Tommaselli, A.M.G., Marcato Junior, J., Honkavaara, E., 2018c. Geometric model and assessment of a dual-fisheye imaging system. *The Photogrammetric Record* 33, 243–263. https://doi.org/10.1111/phor.12240

Castanheiro, L.F., Tommaselli, A.M.G., Berveglieri, A., Campos, M.B., Junior, J.M., 2021. Modeling Hyperhemispherical Points and Calibrating a Dual-Fish-Eye System for Close-Range Applications. *Photogrammetric Engineering and Remote Sensing* 87, 375–384. https://doi.org/10.14358/PERS.87.5.375

Corso, N., Zakhor, A., 2013. Indoor Localisation Algorithms for an Ambulatory Human Operated 3D Mobile Mapping System. *Remote Sensing* 5, 6611–6646. https://doi.org/10.3390/rs5126611

Courbon, J., Mezouar, Y., Eck, L., Martinet, P., 2007. A generic fisheye camera model for robotic applications, in: *IEEE International Conference on Intelligent Robots and Systems*. pp. 1683–1688.

Eising, C., Horgan, J., Yogamani, S., 2022. Near-Field Perception for Low-Speed Vehicle Automation Using Surround-View Fisheye Cameras. *IEEE Trans. Intell. Transport. Syst.* 23, 13976–13993. https://doi.org/10.1109/TITS.2021.3127646.

Flögel, D., Bhatt, N.P., Hashemi, E., 2022. Infrastructure-Aided Localisation and State Estimation for Autonomous Mobile Robots. *Robotics* 11, 82. https://doi.org/10.3390/robotics11040082

Gao, W., Wang, K., Ding, W., Gao, F., Qin, T., Shen, S., 2020. Autonomous aerial robot using dual-fisheye cameras. *J. Field Robotics* 37, 497–514. https://doi.org/10.1002/rob.21946

Geyer, C., Daniilidis, K., 2000. A Unifying Theory for Central Panoramic Systems and Practical Implications, in: Vernon, D. (Ed.), Computer Vision — ECCV 2000, Lecture Notes in Computer Science. Springer Berlin Heidelberg, Berlin, Heidelberg, pp. 445–461. https://doi.org/10.1007/3-540-45053-X_29

GoPro, 2023. GoPro MAX 360 Action Camera [WWW Document]. URL https://gopro.com/en/us/shop/cameras/max/CHDHZ-202-master.html (accessed 2.11.23).

Heng, L., Choi, B., Cui, Z., Geppert, M., Hu, S., Kuan, B., Liu, P., Nguyen, R., Yeo, Y.C., Geiger, A., Lee, G.H., Pollefeys, M., Sattler, T., 2019. Project AutoVision: Localisation and 3D Scene Perception for an Autonomous Vehicle with a Multi-Camera System, in: *2019 International Conference on Robotics and Automation (ICRA)*., Montreal, QC, Canada, pp. 4695–4702. https://doi.org/10.1109/ICRA.2019.8793949

Hughes, C., Denny, P., Jones, E., Glavin, M., 2010. Accuracy of fish-eye lens models. *Appl. Opt.* 49, 3338–3347. https://doi.org/10.1364/AO.49.003338

Insta360, 2023. Insta360, Action Cameras [WWW Document]. URL https://www.insta360.com/ (accessed 2.11.23).

Ji, S., Qin, Z., Shan, J., Lu, M., 2020. Panoramic SLAM from a multiple fisheye camera rig. *ISPRS Journal of Photogrammetry and Remote Sensing* 159, 169–183. https://doi.org/10.1016/j.isprsjprs.2019.11.014

Kedzierski, M., Walczykowski, P., Kaczynski, R., 2006. Precise calibration of fisheye lens camera system and projection model, in: *Annual Conference of the American Society for Photogrammetry and Remote Sensing 2006: Prospecting for Geospatial Information Integration*. pp. 673–677.

Khomutenko, B., Garcia, G., Martinet, P., 2016. An Enhanced Unified Camera Model. *IEEE Robot. Autom. Lett.* 1, 137–144. https://doi.org/10.1109/LRA.2015.2502921

Kim, B., 2013. Indoor Localisation and Point Cloud Generation for Building Interior Modeling, in: *Proceedings - IEEE International Workshop on Robot and Human Interactive Communication.* https://doi.org/10.1109/ROMAN.2013.6628442

Kim, H.S., Kim, Y., Kim, C., Choi, K.H., 2021. Kinematic In Situ Self-Calibration of a Backpack-Based Multi-Beam LiDAR System. *Applied Sciences* 11, 945. https://doi.org/10.3390/app11030945

Koehl, M., Delacourt, T., Boutry, C., 2016. Image capture with synchronised multiple-cameras for extraction of accurate geometries. *Int. Arch. Photogramm. Remote Sens. Spatial Inf. Sci*. XLI-B1, 653–660. https://doi.org/10.5194/isprsarchives-XLI-B1-653-2016

Liang, J.Z., Corso, N., Turner, E., Zakhor, A., 2013. Image Based Localisation in Indoor Environments, in: *2013 Fourth International Conference on Computing for Geospatial Research and Application*. IEEE, San Jose, CA, USA, pp. 70–75. https://doi.org/10.1109/COMGEO.2013.11

Lichti, D.D., Tredoux, W., Maalek, R., Helmholz, P., Radovanovic, R., 2021. Modelling extreme wide-angle lens cameras. *The Photogrammetric Record* 36, 360–380. https://doi.org/10.1111/phor.12389

Lin, Y., Gao, F., Qin, T., Gao, W., Liu, T., Wu, W., Yang, Z., Shen, S., 2018. Autonomous aerial navigation using monocular visual-inertial fusion. *J. Field Robotics* 35, 23–51. https://doi.org/10.1002/rob.21732

Martins, P.F., Costelha, H., Bento, L.C., Neves, C., 2020. Monocular Camera Calibration for Autonomous Driving — a comparative study, in: 2*020 IEEE International Conference on Autonomous Robot Systems and Competitions (ICARSC)*., IEEE, Ponta Delgada, Portugal, pp. 306–311. https://doi.org/10.1109/ICARSC49921.2020.9096104

Meyer, D.E., Lo, E., Klingspon, J., Netchaev, A., Ellison, C., Kuester, F., 2020. TunnelCAM- A HDR Spherical Camera Array for Structural Integrity Assessments of Dam Interiors. *Eletronic Imaging,* 32, 227-1-227–8. https://doi.org/10.2352/ISSN.2470-1173.2020.7.ISS-227

Perfetti, L., Fassi, F., 2022. Handheld fisheye multicamera system: surveying meandering architectonic spaces in open-loop mode – accuracy assessment. *Int. Arch. Photogramm. Remote Sens. Spatial Inf. Sci.* XLVI-2/W1-2022, 435–442. https://doi.org/10.5194/isprs-archives-XLVI-2-W1-2022-435-2022

Perfetti, L., Polari, C., Fassi, F., Troisi, S., Baiocchi, V., Del Pizzo, S., Giannone, F., Barazzetti, L., Previtali, M., Roncoroni, F., 2018. Fisheye Photogrammetry to Survey Narrow Spaces in Architecture and a Hypogea Environment. https://doi.org/10.3390/books978-3-03842-685-1-1

Pernechele, C., 2016. Hyper hemispheric lens. *Opt. Express* 24, 5014. https://doi.org/10.1364/OE.24.005014

Rau, J.Y., Su, B.W., Hsiao, K.W., Jhan, J.P., 2016. Systematic calibration for a backpacked spherical photogrammetry imaging system. *Int. Arch. Photogramm. Remote Sens. Spatial Inf. Sci.* XLI-B1, 695–702. https://doi.org/10.5194/isprsarchives-XLI-B1-695-2016

Ricoh, 2023. 360-degree camera RICOH THETA [WWW Document]. URL https://theta360.com/en/ (accessed 2.11.23).

Schneider, D., Schwalbe, E., Maas, H.-G., 2009. Validation of geometric models for fisheye lenses. *ISPRS Journal of Photogrammetry and Remote Sensing* 64, 259–266.

Schwalbe, E., 2005. Geometric modelling and calibration of fisheye lens camera systems. I*nternational Archives of the Photogrammetry, Remote Sensing and Spatial Information Sciences* XXXVI-5/W8.

Sun, Z., Zhang, Y., 2019. Accuracy Evaluation of Videogrammetry Using A Low-Cost Spherical Camera for Narrow Architectural Heritage: An Observational Study with Variable Baselines and Blur Filters. *Sensors* 19, 496. https://doi.org/10.3390/s19030496

Usenko, V., Demmel, N., Cremers, D., 2018. The Double Sphere Camera Model, in: 2*018 International Conference on 3D Vision (3DV)*, IEEE, Verona, pp. 552–560. https://doi.org/10.1109/3DV.2018.00069